**Journal of Oceanology and Limnology**
**Vol. 44, No. 2, pp. 560-569, 2026**
**https://doi.org/10.1007/s00343-025-4352-5**

Research Paper

# Seasonal cycles of the ocean bottom pressure in the South China Sea and the Luzon Strait deepwater overflow*

Guijun LIU[1, 2], Yu WANG[3, **]

[1] *Frontiers Science Center for Deep Ocean Multispheres and Earth System, Key Laboratory of Physical Oceanography, Ocean University of China, Qingdao 266100, China*
[2] *College of Oceanic and Atmospheric Sciences, Ocean University of China, Qingdao 266100, China*
[3] *National Marine Environmental Monitoring Center, Dalian 116023, China*

Received Dec. 23, 2024; accepted in principle Apr. 11, 2025; accepted for publication Jun. 6, 2025


**Abstract** Driven by the persistent baroclinic pressure difference, the Luzon Strait deepwater overflow (LSDO) from the Pacific into the South China Sea (SCS) plays an influential role in the dynamical processes in the deep SCS. Based on the ocean bottom pressure (OBP) data, seasonal cycles of the OBP anomalies in the SCS and the LSDO are presented. On the seasonal scale, for shelf areas shallower than 200 m, the OBP anomalies are regulated by the wind stress curls: negative curls in winter lead to the Ekman convergences and the ensuing positive OBP anomalies and vice versa for positive curls in summer, while for the deep basin deeper than 2 000 m, the OBP anomalies show spatial consistency in sign: negative in winter and spring as well as positive in summer and autumn. The seasonal cycle of the LSDO is revealed and found to be mainly due to baroclinic processes east of the Luzon Strait. Along 21.25°N, significant seasonal signals extend downward and westward, reaching about 2 500-m depth at 124°E, and phase isolines are parallel to this extending. These facts suggest that the seasonal variability of the LSDO might originate from the upper ocean and meridional mode Rossby waves could be a possible dynamical mechanism.

**Keyword**: seasonal cycle; ocean bottom pressure (OBP); South China Sea (SCS); Luzon Strait deepwater overflow (LSDO); vertically propagating Rossby wave

## 1 INTRODUCTION

The South China Sea (SCS) is the largest marginal sea in the western Pacific Ocean (Fig.1), covering an area of over $3.5\times10^6$ km$^2$ (Chu et al., 1999). As a semi-closed basin, exchanges with surrounding waters are mainly made possible through straits and the Luzon Strait is the only deep connection. Due to strong diapycnal mixing in the deep SCS (Tian et al., 2009; Yang et al., 2016), there exists a persistent baroclinic pressure gradient. And below 1 500 m, the persistent baroclinic pressure gradient across the Luzon Strait drives a deepwater inflow from the Pacific into the SCS (Qu et al., 2006; Tian et al., 2006; Zhou et al., 2014), namely, the Luzon Strait deepwater overflow (LSDO).

By carrying heat and mass from the Pacific, the LSDO significantly influences dynamical processes in the deep SCS. Lan et al. (2013) revealed the driving role of the LSDO in the generation of the basin-scale cyclonic circulation in the deep SCS: the positive potential vorticity (PV) from the LSDO generates a cyclonic circulation in order that the PV balance is satisfied. Zhou et al. (2014) delivered the seasonal variability of the LSDO, which intensifies in late autumn (October–December) and weakens in spring (March–May). And the deep SCS circulation displays a noticeable seasonal variation due to the seasonal variability of the LSDO (Lan et al., 2015). Mixing in the deep SCS is considered to be responsible for the seasonal LSDO variability (Zhou

* Supported by the Research of Key Support Measurement Technology System for Global Change and Air-Sea Interaction (No. GASI-02-ZL-02)
** Corresponding author: yuwang@nmemc.org.cn

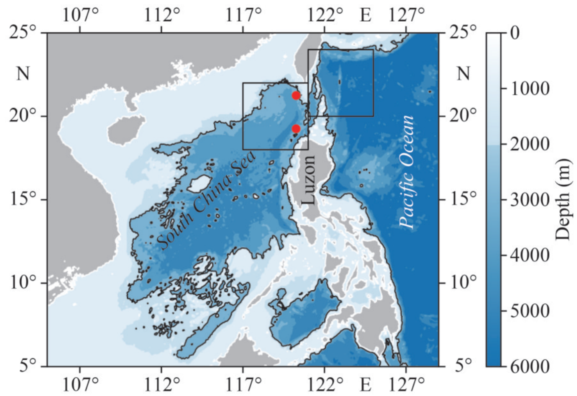


**Fig.1 Bottom topography of the SCS**

The red dots (120.25°E, 21.25°N; 120.25°E, 19.25°N) denote the locations of the OBP anomaly to estimate the LSDO transport anomaly. Squares marked with thick black lines in the Pacific (121°E–125°E, 20°N–24°N) and the SCS (117°E–121°E, 18°N–22°N) are selected to calculate the Pacific-SCS OBP anomaly difference (data in the Pacific minus data in the SCS). The black contours indicate the 2 000-m isobath.

et al., 2014). However, the LSDO is driven by the pressure gradient across the Luzon Strait. Consequently, the contribution of processes east of the Luzon Strait should be discussed.

Ocean bottom pressure (OBP) is the sum of air and water masses above the seafloor, and thus is closely related to the atmospheric and oceanic processes. The launch of the Gravity Recovery and Climate Experiment (GRACE) twin satellites provides detailed measurements of OBP and allows insight into relevant dynamical processes based on the satellite observations, e.g., the strengthened flow of the North Atlantic Deep Water in the interior (Koelling et al., 2020). By comparing the LSDO transport anomaly inferred from OBP with mooring observations, Zhu et al. (2022) proved that the OBP data is deemed suitable and useful for the investigation of the LSDO variability.

Based on the OBP data, we focus on the seasonal cycles of the OBP anomalies in the SCS and the LSDO and attempt to provide a possible dynamical explanation for the seasonal variability of the LSDO. The rest of this article is organized as follows. Section 2 describes the data and methods. Results are carefully analyzed in Section 3 and discussed in Section 4, followed by conclusions in Section 5.

## 2 MATERIAL AND METHOD

### 2.1 Data

The OBP data adopted in this article spans from January 1992 to December 2017 together with the spatial resolution of 0.5°×0.5° and is obtained from the Estimating the Circulation and Climate of the Ocean version 4 release 4 (ECCOv4r4, hereinafter ECCO), which assimilates the GRACE OBP data, satellite altimetry data, in-situ observations and many other available observational data sources (Forget et al., 2015). With the global mean air pressure removed, the ECCO OBP is converted to the thickness of the water column in meters (1 mm of OBP corresponds to roughly 10 Pa). Since the main interest here is in the seasonal variability, the downloaded daily ECCO data is first averaged to produce the monthly data. As pointed out by Johnson and Chambers (2013), the OBP data consists of a linear trend of approximately 2 cm per decade, and consequently linear detrending is performed prior to our analysis.

The monthly surface wind data from the fifth-generation European Centre for Medium-Range Weather Forecasts Reanalysis (ERA5) product from 1992 to 2017 with the spatial resolution of 0.25°× 0.25° (Hersbach et al., 2020) is also used in this study.

### 2.2 Method

For large scale flows in which the geostrophic balance dominates, volume transport can be determined by integrating the geostrophic balance equations. A relation between the meridional transport of North Atlantic meridional overturning circulation and the OBP at the boundaries is established by Bingham and Hughes (2008):

$$T=\frac{p_{\mathrm{E}}-p_{\mathrm{W}}}{\rho_0 f}, \tag{1}$$

where $T$ is the northward volume transport, $\rho_0$ the mean water density, $f$ the Coriolis parameter, and $p_{\mathrm{E}}$ and $p_{\mathrm{W}}$ the OBP at the eastern boundary and western boundary, respectively. Bingham and Hughes (2009) furtherly highlighted the efficacy of estimating the meridional transport with the east-west OBP difference across the basin. With the vertical integration of Eq.1 between depth levels $z$=3 000 m and $z$=5 000 m, Landerer et al. (2015) discussed the long-term variability of the Lower North Atlantic Deep Water transport.

Since the LSDO is basically geostrophic (e.g., Tian et al., 2006), its zonal transport can also be calculated in a similar way (as shown in Zhu et al. (2022)):

$$Q=\int_{H_2}^{H_1}\frac{p_{\mathrm{N}}-p_{\mathrm{S}}}{\rho_0 f}\,\mathrm{d}z, \tag{2}$$

where $Q$ represents the LSDO transport (positive value for the westward transport), $H_1$ the upper interface of the LSDO, $H_2$ its lower interface, $p_N$ and $p_S$ the OBP at the northern boundary and southern boundary respectively. To avoid the hydrological signal leakage, the locations of $p_N$ and $p_S$ are selected to be relatively far from land, 120.25°E, 21.25°N and 120.25°E, 19.25°N respectively (red circles in Fig.1). $H_1$–$H_2$, taken to be 850 m, denotes the mean thickness of the LSDO, i.e., from the bifurcation depth (~1 500 m) to the deepest sill depth in the Bashi Channel (~2 400 m).

Complex Empirical Orthogonal Function (CEOF) analysis enables one to identify propagating features. A complex field $Y(x, y, t)$ is firstly constructed with the original field $X(x, y, t)$ by adding its Hilbert transform $H[X(x, y, t)]$ times the imaginary unit $i$, i.e., $Y(x, y, t)=X(x, y, t)+iH[X(x, y, t)]$. Due to the orthogonality of the imaginary and real parts of $Y$, the CEOF analysis is capable of isolating patterns of variability that propagate both in time and space. Then, a standard decomposition is conducted as in the Empirical Orthogonal Function analysis:

$$Y\left(x,y,t\right) = \sum_{j=1}^{n} A_j(t)\, B_j^*\left(x,y\right), \tag{3}$$

where $A$ means the principal component, $B$ the spatial pattern and asterisk (*) the complex conjugate operator. The spatial amplitude $S_j$, spatial phase $\varphi_j$, temporal amplitude $R_j$ and temporal phase $\phi_j$ of the $j^{\text{th}}$ CEOF mode are hereby defined:

$$\begin{cases} S_j = \sqrt{B_j B_j^*} \\ \phi_j = \tan^{-1}\dfrac{\mathrm{Im}\left(B_j\right)}{\mathrm{Re}\left(B_j\right)} \\ R_j = \sqrt{A_j A_j^*} \\ \varphi_j = \tan^{-1}\dfrac{\mathrm{Im}\left(A_j\right)}{\mathrm{Re}\left(A_j\right)} \end{cases}, \tag{4}$$

where Im() and Re() correspond to respectively the imaginary and real parts. The spatial phase shows the propagating structure, and the temporal phase measures the temporal variation (Barnett, 1983; Hannachi et al., 2007).

Harmonic analysis is also applied to quantify seasonal variations (detailed information about harmonic analysis can be found in Liu and Lan (2022)).

### 2.3 Meridional mode Rossby waves

For large-scale Rossby waves with low-frequency and low-wavenumber, the dispersive relation for the meridionally standing wave modes is:

$$\omega = -\frac{kc}{2l+1}, \tag{5}$$

where $\omega$ is the frequency, $k$ the zonal wavenumber and $l$ the meridional mode number. Equation 5 is furtherly simplified under the Wentzel-Kramers-Brillouin (WKB) approximation:

$$\omega = -\frac{kN}{m(2l+1)}, \tag{6}$$

where $N$ is the background buoyancy frequency and $m=N/c$ is the local vertical wavenumber. And the slope of ray paths is given:

$$\frac{\mathrm{d}z}{\mathrm{d}x} = \frac{\mathrm{d}z/\mathrm{d}t}{\mathrm{d}x/\mathrm{d}t} = \frac{\partial\omega}{\partial m}\Big/\frac{\partial\omega}{\partial k} = -\frac{k}{m} = \frac{\omega(2l+1)}{N}. \tag{7}$$

Ray paths would be steeper for weaker stratification or higher order modes. The slope of phase isolines is also $-k/m$, equal to the right side of Eq.7, indicating that phase isolines are parallel to the WKB ray paths. Hence, energy from the surface propagates downward to the west along the ray paths while its phase propagates upward to the west across the ray paths (McCreary, 1984; Kessler and McCreary, 1993).

Each mode has its own meridional structure. For the zonal velocity, the structure function $U_l$ is:

$$U_l = i\frac{\sqrt{\beta c}}{\omega}\left[\frac{\sqrt{\frac{l+1}{2}}}{1-\frac{kc}{\omega}}\frac{H_{l+1}(\eta)e^{-\frac{\eta^2}{2}}}{\pi^{\frac{1}{4}}\sqrt{2^{l+1}(l+1)!}} + \frac{\sqrt{\frac{l}{2}}}{1+\frac{kc}{\omega}}\frac{H_{l-1}(\eta)e^{-\frac{\eta^2}{2}}}{\pi^{\frac{1}{4}}\sqrt{2^{l-1}(l-1)!}}\right], \tag{8}$$

where $H_l(\eta)$ is the $l^{\text{th}}$ order Hermite polynomial, $\eta=y(\beta/c)^{0.5}$, $\beta$ the meridional changing rate Coriolis parameter (Ishizaki et al., 2014). As $l$ grows larger, the meridional mode Rossby waves are less equatorially trapped and oscillate within wider latitudinal ranges. Low order modes dominate in the equatorial ocean while high order modes become prominent in higher latitudes.

## 3 RESULT

### 3.1 The OBP seasonal cycle

The seasonal cycle of the OBP anomalies in the SCS is illustrated in Fig.2, where January, April,

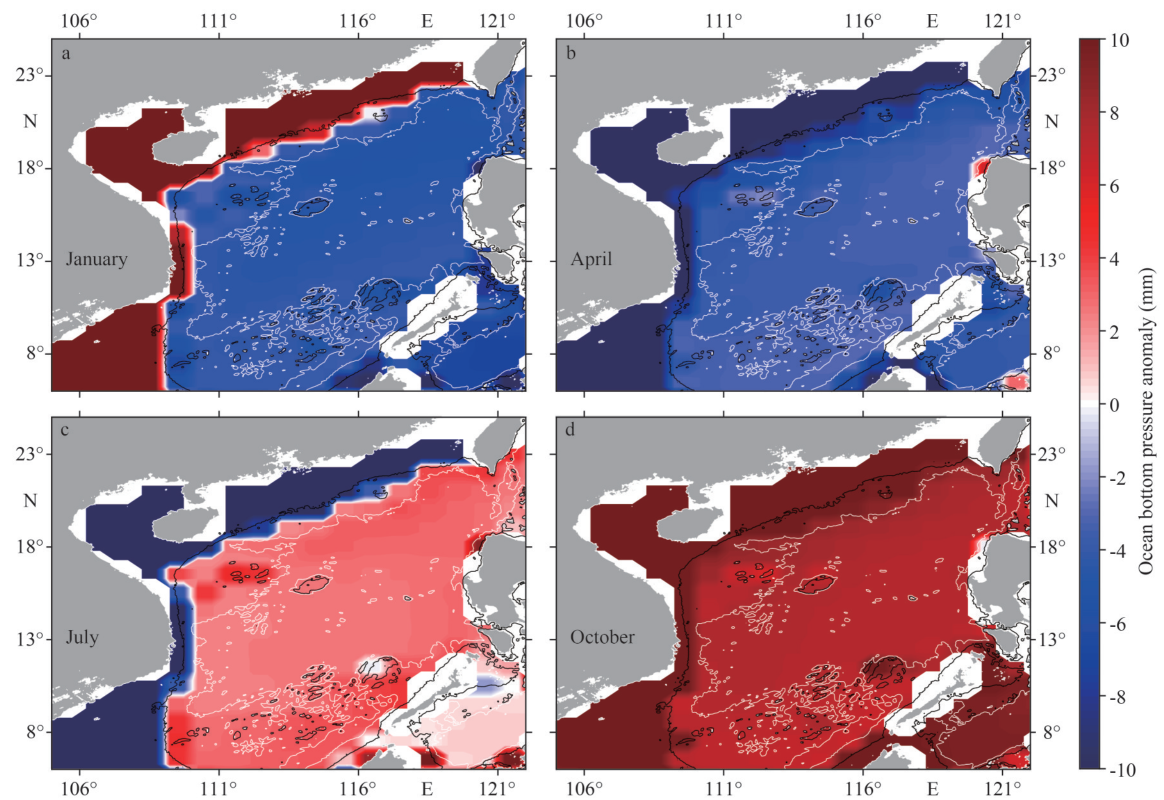


**Fig.2 The monthly mean OBP anomalies in the SCS in different seasons**

a. January for winter; b. April for spring; c. July for summer; d. October for autumn. The black and white contours denote the 200- and 2 000-m isobaths, respectively.

July, and October are chosen to represent winter, spring, summer, and autumn, respectively. The significant seasonal variability of the OBP anomalies in the SCS is clearly exhibited, with the amplitude of up to 10 cm in the continental shelf regions (shallower than 200 m) and about 8 mm in the deep basin (deeper than 2 000 m). In winter, the OBP shows positive anomalies in the continental shelf regions and negative anomalies in the deep basin (Fig.2a), while in summer, this pattern is reversed (Fig.2c). Basically, the OBP anomalies are spatially consistent in sign during transitional seasons: negative in spring and positive in autumn in the whole SCS (Fig.2b & d).

Due to the removal of the air pressure load in the ECCO OBP data, the OBP anomaly results from the convergence and divergence of seawater transport. A convergence would lead to an increase of water mass over the seafloor, that is, a positive OBP anomaly, and vice versa for a divergence. For the shelf regions, e.g., the northern shelf area of the SCS and waters off the Vietnam coast, the prevailing northeast monsoon in winter leads to negative wind stress curls and convergences of the Ekman transport; therefore, positive OBP anomalies emerge there. In summer, the southwest monsoon reverses the pattern to negative OBP anomalies. However, cases are not the same for the deep basin. Although both negative and positive curls can be found over the deep basin throughout the four seasons, the OBP anomalies remain nearly spatially consistent, indicative of a different mechanism. Considering the role of the LSDO in driving the cyclonic abyssal SCS circulation and contributing to its seasonal variability (Lan et al., 2013, 2015), the seasonal variation of the OBP anomalies in the deep SCS basin may be attributed to the seasonal variation of the LSDO.

### 3.2 The LSDO anomaly

Based on Eq.2, the LSDO transport anomaly is determined with the ECCO OBP data (Fig.3). The 12 years of continuous observation gives the LSDO transport of 0.84±0.39 Sv (Zhou et al., 2023; 1 Sv= $10^6$ m$^3$/s), and our calculation shows a standard deviation of 0.40 Sv. On the seasonal time scale, the LSDO transport anomaly increases from April to November and is in a decreasing phase from

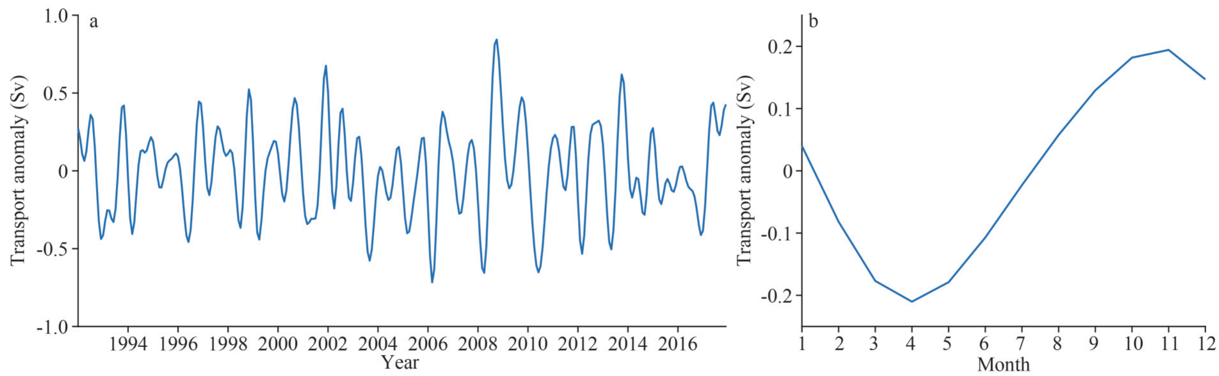


**Fig.3 The LSDO transport anomaly estimated by Eq.2**

a. the time series; b. the annual cycle.

November to April of the following year, reaching its minimum in April and maximum in November (Fig.3b). The annual cycle of the transport anomaly with a standard deviation of 0.40 Sv, which peaks in late autumn and reaches its minimum in spring, is in good agreement with the mooring observations in Zhou et al. (2014), suggesting our estimate to be effective in exploring the seasonal variability of the LSDO.

The LSDO is driven by the baroclinic pressure gradient across the Luzon Strait (Qu et al., 2006). Apparently, the seasonal variation of the pressure difference across the Luzon Strait should be responsible for the seasonal variation of the LSDO. With the hydraulic theory (Qu et al., 2006; Zhu et al., 2022), a new estimate of the LSDO transport anomaly (figure not shown) is calculated with the OBP anomaly difference between the Pacific and the SCS (121°E–125°E, 20°N–24°N and 117°E–121°E, 18°N–22°N, respectively; boxes in Fig.1). The correlation coefficient between the two estimated LSDO transport anomaly time series reaches 0.6, and as a matter of fact, the new estimate is favorably comparable with the former estimate shown in Fig.3. Although the new estimation based on the hydraulic theory relies on the area choices to calculate the Pacific-SCS OBP anomaly difference, it does not prevent from demonstrating the seasonal variability of the LSDO and the consistency with the estimate by Eq.2. Furtherly, the seasonal variations of the OBP anomalies east (121°E–125°E, 20°N–24°N) and west of the Luzon Strait (117°E–121°E, 18°N–22°N) are quantified using harmonic analysis: 2.1 and 0.73 mm respectively. These results indicate that the seasonal variability of the OBP anomalies in the Pacific is more significant than those in the SCS and dominates the seasonal variability of the LSDO.

# 4 DISCUSSION

## 4.1 Seasonal variability of the LSDO

Previous studies have already focused on the seasonal OBP variability and have discussed its dynamical mechanism (e.g., Ponte, 1999; Song and Qu, 2011). Under the assumption of Sverdrup dynamics in the interior ocean and Ekman dynamics near the surface, Gill and Niller (1973) derived a dynamical framework for the OBP:

$$J\left(p_{\mathrm{b}}, \frac{H}{\sin\theta}\right) = J\left(\frac{1}{\sin\theta}, P\right) - 2\Omega\rho_0 w_{\mathrm{E}}, \tag{9}$$

where $p_{\mathrm{b}}$ is the OBP; $H$ is the depth; $J$ is a Jacobian term defined by $J(C, D)=(C_\lambda D_\theta - C_\theta D_\lambda)/(a^2\cos\theta)$; $\theta$ is the latitude; $\lambda$ is the longitude; $a$ and $\Omega$ are the Earth's radius and rotation rate, respectively; $w_{\mathrm{E}}$ is the Ekman pumping velocity; and the potential energy of the water column per unit area $P$ is:

$$P = \int_H^0 \rho g z \mathrm{d}z, \tag{10}$$

where $\rho$ is the water density and g the gravitational acceleration. The two terms on the right side of Eq.9 denote baroclinic processes associated with density changes (hereafter the baroclinic term) and forcing by the wind stress curl (hereafter the Ekman term, including the negative sign). Thus, the variability of OBP (the Jacobian term) is interpreted as a superposition of the baroclinic term (baroclinic contribution related to the density variations) and the Ekman term (barotropic contribution by the wind stress curl). For the seasonal OBP variability, baroclinic processes take the leading role in equatorial regions and the Ekman term predominates in higher latitudes (Gill and Niller, 1973; Piecuch et al., 2015; Chen et al., 2023).

Using Eq.9, the averaged Jacobian terms and

Ekman terms in the central North Pacific (150°E–155°E, 20°N–30°N) and east of the Luzon Strait are displayed (Fig.4). In the central North Pacific, the Jacobian term and the Ekman term have a high correlation rate of 0.66 and their annual cycles are in phase with a 1-month lag (Fig.4c, d), demonstrating that the seasonal variation of the wind stress curl dominates the seasonal OBP changes. On the other hand, for the region east of the Luzon Strait, the correlation coefficient drops to 0.31 (Fig.4a). On the seasonal time scale (Fig.4b), the Jacobian term is at its minimum in spring (April) and maximum in late autumn (October) with an increasing phase in between, consistent with the annual cycle of the LSDO (Fig.2b), while the Ekman term peaks in summer (August) and attains a minimum in winter (February). Comparing Fig.4a, b with Fig.4c, d, it is clear that although the wind stress curl plays its role in regulating the seasonal OBP variability in the central North Pacific, agreeing with the previous studies, baroclinic processes may be of more importance for the region east of the Luzon Strait. That is, the seasonal variability of the baroclinic pressure east of the Luzon Strait should be vital to the seasonal variability of the LSDO, in agreement with Xu et al. (2023).

### 4.2 Vertical propagation

Seasonal variations in the deep ocean can be attributed to the surface wind forcing through the vertically propagating Rossby waves, which has been extensively studied in the equatorial areas (Thierry et al. (2006) for the Atlantic, Ishizaki et al. (2014) for the Pacific, Huang et al. (2018) for the Indian Ocean), e.g., the annual reversal of the Equatorial Intermediate Current is ascribed to the first order meridional mode Rossby waves (Marin et al., 2010; Luo et al., 2024). And higher order modes could explain the contribution of the SCS monsoon to the seasonal variations in the deep SCS (Liu and Lan, 2022). Similarly, based on Eq.8, the most prominent modes are determined to be 15, 18, 20, 22, 23, 25 at 21.25°N with an assumed zonal wavelength of 6 000 km (from a best fitting of the harmonic phases and zonal distances from 1 500- to 2 400-m depth) and annual period (Fig.5b).

To investigate the propagating features, the CEOF method is applied to the zonal velocity along 21.25°N. The spatial amplitude, spatial phase, temporal amplitude and temporal phase of the 1$^{st}$ CEOF mode, accounting for 60% of the total variability, are presented in Fig.6. Note that the spatial phase is expressed by the month of its positive maximum. Combining Fig.6b & d, the temporal phase varies linearly and shows a quasi-periodic variation except during three time periods (October 2006–December 2006; January 2011–March 2011; February 2014–April 2014), where the temporal amplitude is small. And spectrum analysis reveals a dominant annual variation of the temporal phase (Fig.7). That is, the 1$^{st}$ CEOF mode fully captures the seasonal characteristics along 21.25°N.

For the spatial amplitude (Fig.6a), significant seasonal signals (more than 0.4 cm/s) are confined to the upper ocean and slope downward as well as

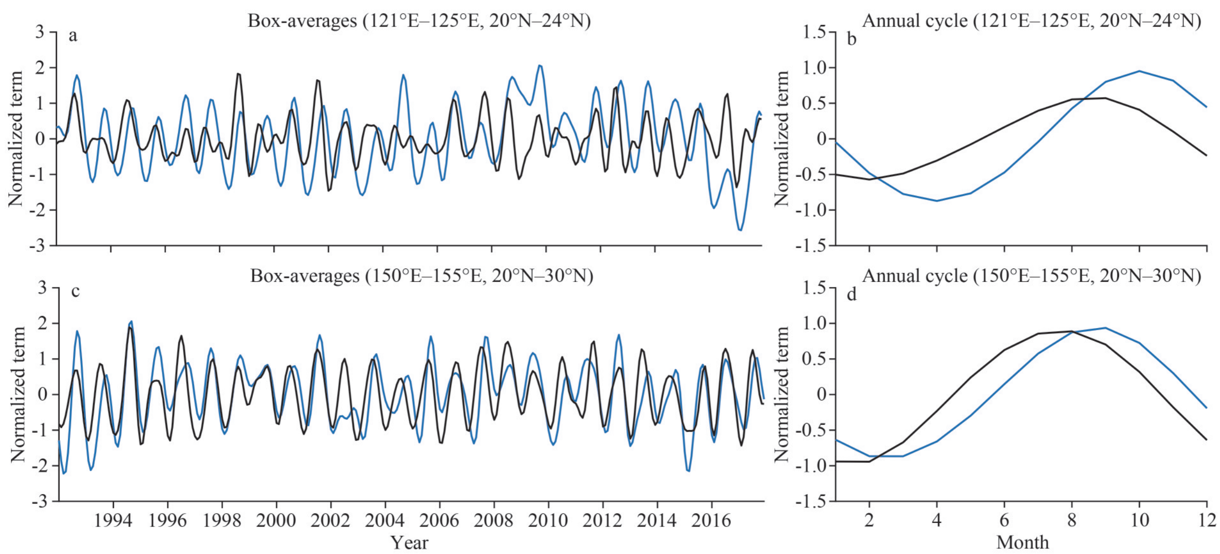


**Fig.4 The normalized Jacobian terms and Ekman terms**

The normalized Jacobian term (blue line (a)) and Ekman term (black line) averaged over the box east of the Luzon Strait (121°E–124°E, 20°N–24°N; shown in Fig.1) and their annual cycles (b). (c) and (d) are similar to (a) and (b) but for a different region in the central North Pacific (150°E–155°E, 20°N–30°N).

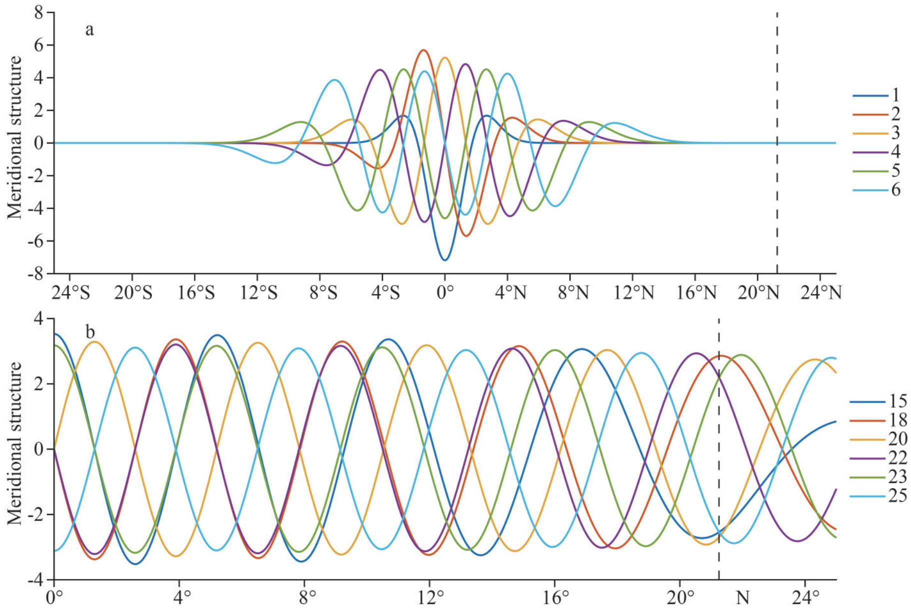


**Fig.5 Meridional structure functions of the zonal velocity *U***

The (a) *l*=1, 2, 3, 4, 5, 6 modes and (b) *l*=15, 18, 20, 22, 23, 25 modes. The black dotted lines denote the 21.25°N.

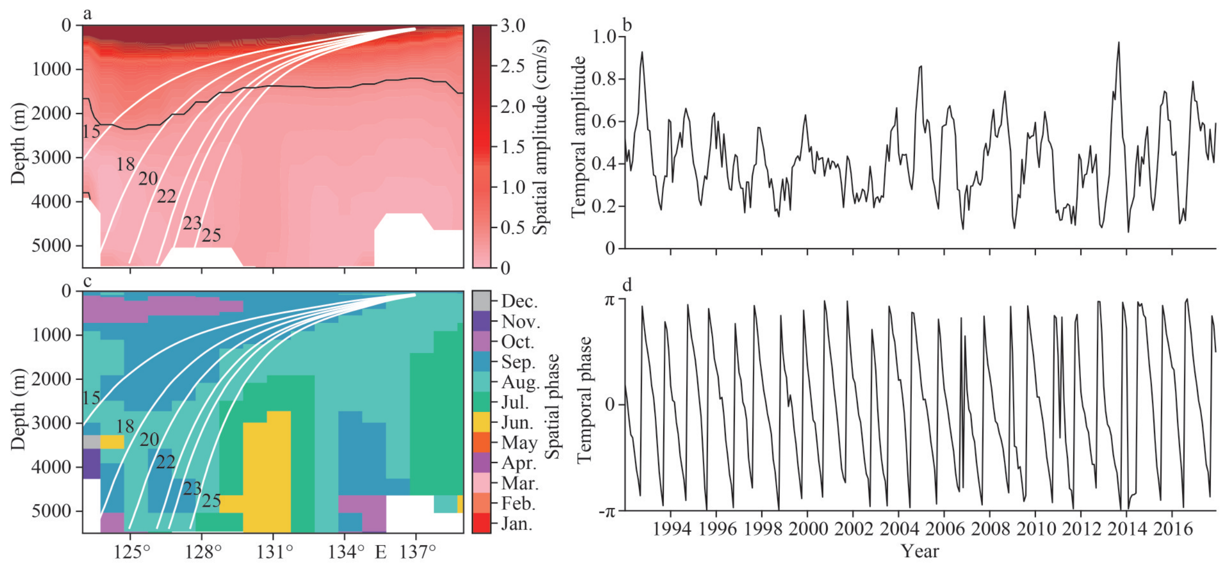


**Fig.6 CEOF decomposition of the zonal velocity along 21.25°N**

The spatial amplitude (a), temporal amplitude (b), spatial phase (c), and temporal phase (d) of the 1st CEOF mode for the zonal velocity from ECCO. Black lines in (a) mark the 0.4-cm/s contours. White lines in (a) and (c) correspond, from top to bottom, to ray paths of the *l*=15, 18, 20, 22, 23, 25 meridional mode Rossby waves.

westward to the depth of about 2 500 m east of the Luzon Strait. The WKB ray path of the *l*=22 mode serves as a dividing line. Below this line, seasonal signals tend to vanish in the deep ocean. Above this line, the spatial amplitude is noticeably stronger with its maximum located at ~100-m depth. And the downward and westward extending of high amplitude is consistent with ray paths of the *l*=15, 18, 20, 22 meridional mode Rossby waves. Meanwhile, the increased spatial phase indicates the propagation direction. The spatial phase is characterized by westward and upward propagation despite its mess in the eastern Philippine basin (Fig.6c), which is clearer above the dividing line. Phase isolines are virtually parallel to those WKB ray paths. In particular, these facts suggest that the vertical propagation of high order mode Rossby waves contributes to the seasonal variability east of

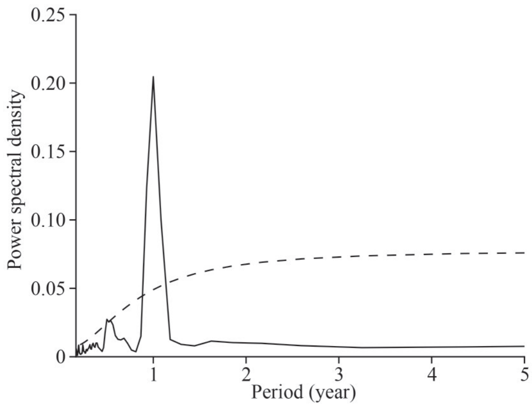


**Fig.7 Power spectrum analysis of the temporal phase of the 1st CEOF mode**

The dashed line marks the 95% confidence level.

the Luzon Strait.

Vertically propagating Rossby waves responsible for seasonal variations in the deep ocean are externally forced by the propagation of the annual zonal wind (Kessler and McCreary, 1993; Marin et al., 2010). To investigate the excitation source, we decompose the zonal wind over the Philippine Sea harmonically, of which the explained variance, amplitude, and phase are illustrated in Fig.8. The distribution of amplitude is similar to that of the explained variance. A standing annual pattern with the maximum of 5 m/s is readily distinguishable in the western and southern Philippine Sea, explaining more than 50% of the total variance, and there are two minimums centered at 149°E, 20°N and 123°E, 29°N respectively. In the meantime, the westward propagating zonal wind is obvious in the northern Philippine Sea (north of 20°N) and along 21.25°N the annual zonal wind propagates westward east of 130°E. Judging from Figs.6 & 8, the westward propagating zonal wind over 130°E–140°E, 20.5°N–23.5°N (black box in Fig.8) is regarded as the excitation source of the annual Rossby waves. Energy by the wind propagates downward to the west along the WKB ray paths through the annual Rossby waves from the eastern upper Philippine Sea.

## 5 CONCLUSION

Based on the ECCO OBP data, annual cycles of the OBP anomalies in the SCS and the LSDO transport anomaly are studied. The seasonal OBP anomaly variation is modulated by the wind stress curls in the continental shelf areas shallower than 200 m: negative curls lead to the convergences of Ekman transport and the ensuing positive OBP anomalies in winter and vice versa for positive curls in summer. For the deep SCS basin deeper than 2 000 m, despite the existence of both positive and negative wind curls, the OBP anomalies are nearly spatially consistent in sign on the seasonal time scale: negative in winter and spring as well as positive in summer and autumn.

The LSDO transport anomaly determined with the ECCO OBP data has a standard deviation of 0.40 Sv and its annual cycle peaks in late autumn and reaches its minimum in spring, consistent with mooring observations. Seasonal variability of the OBP anomaly east of the Luzon Strait, dominated by baroclinic processes in the Pacific, is considered to be

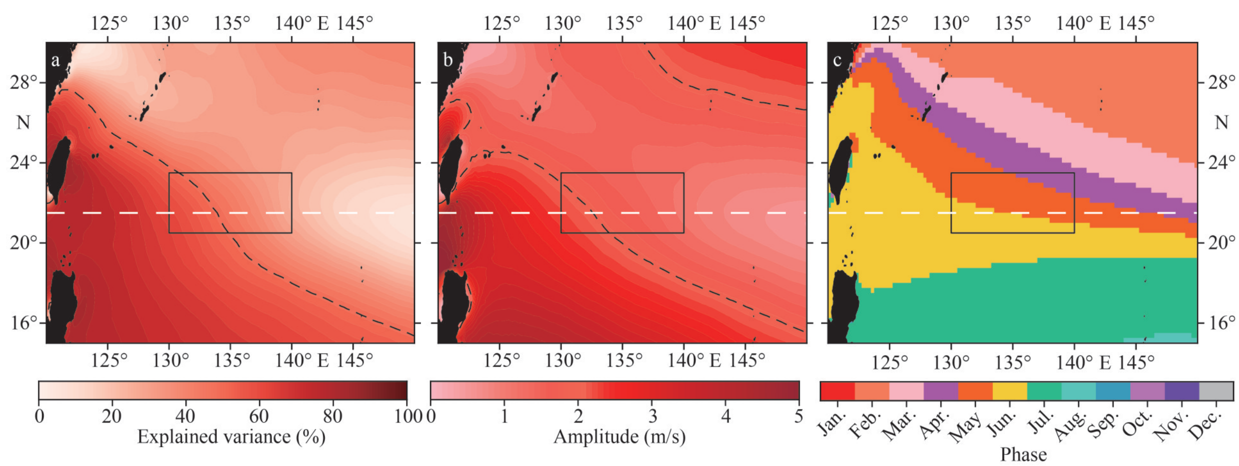


**Fig.8 Annual harmonics of the surface zonal wind over the Philippine Sea explained by the annual zonal wind from the ERA5 reanalysis data**

a. the variance; b. the amplitude; c. the phase. The white dotted lines denote the 21.25°N. The black box (130°E–140°E, 20.5°N–23.5°N) denotes the area of westward propagating annual zonal wind. The black dashed lines in (a) and (b) correspond to the 50% and the 2-m/s contours respectively.

the main cause of the seasonal LSDO variability. Along 21.25°N, the westward and downward extending of seasonal signals is obvious, reaching about 2 500-m depth at 124°E, and the slope of phase isolines, parallel to this extending of amplitude maxima, is consistent with the WKB ray paths. These facts suggest that vertically propagating Rossby waves induced by the annual zonal wind over the eastern Philippine Sea contribute to the seasonal variation of the LSDO.

## 6 DATA AVAILABILITY STATEMENT

The ECCO data analyzed is available at https://data.nas.nasa.gov/ecco/eccodata/llc_90/ECCOv4/Release4/. The monthly ERA5 reanalysis data of the surface wind is downloaded from https://cds.climate.copernicus.eu/datasets/reanalysis-era5-single-levels-monthly-means?tab=overview.

### References


Barnett T P. 1983. Interaction of the monsoon and Pacific Trade Wind system at interannual time scales part I: the equatorial zone. *Monthly Weather Review*, **111**(4): 756-773, https://doi.org/10.1175/1520-0493(1983)111<0756:IOTMAP>2.0.CO;2.

Bingham R J, Hughes C W. 2008. Determining North Atlantic meridional transport variability from pressure on the western boundary: a model investigation. *Journal of Geophysical Research*: *Oceans*, **113**(C9): C09008, https://doi.org/10.1029/2007JC004679.

Bingham R J, Hughes C W. 2009. Geostrophic dynamics of meridional transport variability in the subpolar North Atlantic. *Journal of Geophysical Research*: *Oceans*, **114**(C12): C12029, https://doi.org/10.1029/2009JC005492.

Chen L, Yang J Y, Wu L X. 2023. Topography effects on the seasonal variability of ocean bottom pressure in the North Pacific Ocean. *Journal of Physical Oceanography*, **53**(3): 929-941, https://doi.org/10.1175/JPO-D-22-0140.1.

Chu P C, Edmons N L, Fan C W. 1999. Dynamical mechanisms for the South China Sea seasonal circulation and thermohaline variabilities. *Journal of Physical Oceanography*, **29**(11): 2971-2989, https://doi.org/10.1175/1520-0485(1999)029<2971:DMFTSC>2.0.CO;2.

Forget G, Campin J M, Heimbach P et al. 2015. ECCO version 4: an integrated framework for non-linear inverse modeling and global ocean state estimation. *Geoscientific Model Development*, **8**(10): 3071-3104, https://doi.org/10.5194/gmd-8-3071-2015.

Gill A E, Niller P P. 1973. The theory of the seasonal variability in the ocean. *Deep Sea Research and Oceanographic Abstracts*, **20**(2): 141-177, https://doi.org/10.1016/0011-7471(73)90049-1.

Hannachi A, Jolliffe I T, Stephenson D B. 2007. Empirical orthogonal functions and related techniques in atmospheric science: a review. *International Journal of Climatology*, **27**(9): 1119-1152, https://doi.org/10.1002/joc.1499.

Hersbach H, Bell B, Berrisford P et al. 2020. The ERA5 global reanalysis. *Quarterly Journal of the Royal Meteorological Society*, **146**(730): 1999-2049, https://doi.org/10.1002/qj.3803.

Huang K, McPhaden M J, Wang D X et al. 2018. Vertical propagation of middepth zonal currents associated with surface wind forcing in the equatorial Indian Ocean. *Journal of Geophysical Research*: *Oceans*, **123**(10): 7290-7307, https://doi.org/10.1029/2018JC013977.

Ishizaki H, Nakano H, Nakano T et al. 2014. Evidence of equatorial Rossby wave propagation obtained by deep mooring observations in the western Pacific Ocean. *Journal of Oceanography*, **70**(6): 463-488, https://doi.org/10.1007/s10872-014-0247-3.

Johnson G C, Chambers D P. 2013. Ocean bottom pressure seasonal cycles and decadal trends from GRACE Release-05: ocean circulation implications. *Journal of Geophysical Research*: *Oceans*, **118**(9): 4228-4240, https://doi.org/10.1002/jgrc.20307.

Kessler W S, McCreary J P. 1993. The annual wind-driven Rossby wave in the subthermocline equatorial Pacific. *Journal of Physical Oceanography*, **23**(6): 1192-1207, https://doi.org/10.1175/1520-0485(1993)023<1192:TAWDRW>2.0.CO;2.

Koelling J, Send U, Lankhorst M. 2020. Decadal strengthening of interior flow of North Atlantic Deep Water observed by GRACE satellites. *Journal of Geophysical Research*: *Oceans*, **125**(11): e2020JC016217, https://doi.org/10.1029/2020JC016217.

Lan J, Wang Y, Cui F J et al. 2015. Seasonal variation in the South China Sea deep circulation. *Journal of Geophysical Research*: *Oceans*, **120**(3): 1682-1690, https://doi.org/10.1002/2014JC010413.

Lan J, Zhang N N, Wang Y. 2013. On the dynamics of the South China Sea deep circulation. *Journal of Geophysical Research*: *Oceans*, **118**(3): 1206-1210, https://doi.org/10.1002/jgrc.20104.

Landerer F W, Wiese D N, Bentel K et al. 2015. North Atlantic meridional overturning circulation variations from GRACE ocean bottom pressure anomalies. *Geophysical Research Letters*, **42**(19): 8114-8121, https://doi.org/10.1002/2015GL065730.

Liu G J, Lan J. 2022. Distribution of seasonal signals in the deep South China Sea. *Deep Sea Research Part I*: *Oceanographic Research Papers*, **190**: 103895, https://doi.org/10.1016/j.dsr.2022.103895.

Luo Z P, Yang D Z, Xu L J et al. 2024. Baroclinic Rossby waves with phase lag cause seasonal upward-propagating signals in the mid-depth equatorial Pacific Ocean. *Journal of Geophysical Research*: *Oceans*, **129**(5): e2023JC020418, https://doi.org/10.1029/2023JC020418.

Marin F, Kestenare E, Delcroix T et al. 2010. Annual reversal of the equatorial intermediate current in the Pacific: observations and model diagnostics. *Journal of Physical Oceanography*, **40**(5): 915-933, https://doi.org/10.1175/2009JPO4318.1.

McCreary J P Jr. 1984. Equatorial beams. *Journal of Marine Research*, **42**(2): 395-430, https://doi.org/10.1357/00222

4084788502792.

Piecuch C G, Fukumori I, Ponte R M et al. 2015. Vertical structure of ocean pressure variations with application to satellite-gravimetric observations. *Journal of Atmospheric and Oceanic Technology*, **32**(3): 603-613, https://doi.org/10.1175/JTECH-D-14-00156.1.

Ponte R M. 1999. A preliminary model study of the large-scale seasonal cycle in bottom pressure over the global ocean. *Journal of Geophysical Research*: *Oceans*, **104**(C1): 1289-1300, https://doi.org/10.1029/1998JC900028.

Qu T D, Girton J B, Whitehead J A. 2006. Deepwater overflow through Luzon Strait. *Journal of Geophysical Research*: *Oceans*, **111**(C1): C01002, https://doi.org/10.1029/2005JC003139.

Song Y T, Qu T D. 2011. Multiple satellite missions confirming the theory of seasonal oceanic variability in the northern North Pacific. *Marine Geodesy*, **34**(3-4): 477-490, https://doi.org/10.1080/01490419.2011.590110.

Thierry V, Mercier H, Treguier A M. 2006. Seasonal fluctuations in the deep central equatorial Atlantic Ocean: a data-model comparison. *Ocean Dynamics*, **56**(5-6): 581-593, https://doi.org/10.1007/s10236-005-0045-y.

Tian J W, Yang Q X, Liang X F et al. 2006. Observation of Luzon Strait transport. *Geophysical Research Letters*, **33**(19): L19607, https://doi.org/10.1029/2006GL026272.

Tian J W, Yang Q X, Zhao W. 2009. Enhanced diapycnal mixing in the South China Sea. *Journal of Physical Oceanography*, **39**(12): 3191-3203, https://doi.org/10.1175/2009JPO3899.1.

Xu Q B, Zhang L L, Xiao X et al. 2023. Seasonal link between deepwater overflow through the Luzon Strait and deep western boundary current in the Philippine Sea. *Geophysical Research Letters*, **50**(18): e2023GL105405, https://doi.org/10.1029/2023GL105405.

Yang Q X, Zhao W, Liang X F et al. 2016. Three-dimensional distribution of turbulent mixing in the South China Sea. *Journal of Physical Oceanography*, **46**(3): 769-788, https://doi.org/10.1175/JPO-D-14-0220.1.

Zhou C, Xiao X, Zhao W et al. 2023. Increasing deep-water overflow from the Pacific into the South China Sea revealed by mooring observations. *Nature Communications*, **14**(1): 2013, https://doi.org/10.1038/s41467-023-37767-4.

Zhou C, Zhao W, Tian J W et al. 2014. Variability of the deep-water overflow in the Luzon Strait. *Journal of Physical Oceanography*, **44**(11): 2972-2986, https://doi.org/10.1175/JPO-D-14-0113.1.

Zhu Y H, Yao J X, Xu T F et al. 2022. Weakening trend of Luzon Strait overflow transport in the past two decades. *Geophysical Research Letters*, **49**(7): e2021GL097395, https://doi.org/10.1029/2021GL097395.